coatings

MDPI

Article

Influence of TiC Addition on Corrosion and Tribocorrosion Resistance of Cr_2Ti-NiAl Electrospark Coatings

Konstantin A. Kuptsov [1], Mariya N. Antonyuk [1], Alexander N. Sheveyko [1], Andrey V. Bondarev [2,*] and Dmitry V. Shtansky [1]

[1] National University of Science and Technology "MISIS", Leninsky prospect 4, Moscow 119049, Russia
[2] Department of Control Engineering, Faculty of Electrical Engineering, Czech Technical University in Prague, Technicka 2, Prague 6, 16627 Prague, Czech Republic
* Correspondence: bondaan2@fel.cvut.cz

Abstract: Marine and coastal infrastructures usually suffer from synergetic effect of corrosion and wear known as tribocorrosion, which imposes strict requirements on the structural materials used. To overcome this problem, novel composite wear- and corrosion-resistant xTiC-Fe-CrTiNiAl coatings with different TiC content were successfully developed. The coatings were obtained by the original technology of electrospark deposition in a vacuum using xTiC-Cr_2Ti-NiAl (x = 0, 25, 50, 75%) electrodes. The structure and morphology of the coatings were studied in detail by XRD, SEM, and TEM. The effect of TiC content on the tribocorrosion behavior of the coatings was estimated using tribological and electrochemical (under stationary and wear conditions) experiments, as well as impact testing, in artificial seawater. The TiC-free Fe-Cr_2Ti-NiAl coating revealed a defective inhomogeneous structure with transverse and longitudinal cracks. Introduction of TiC allowed us to obtain coatings with a dense structure without visible defects and with uniformly distributed carbide grains. The TiC-containing coatings were characterized by a hardness and elastic modulus of up to 10.3 and 158 GPa, respectively. Formation of a composite structure with a heavily alloyed corrosion-resistant matrix based on α-(Fe,Cr) solid solution and uniformly distributed TiC grains led to a significant increase in resistance to stationary corrosion and tribocorrosion in artificial seawater. The best 75TiC-Fe-CrTiNiAl coating demonstrated the lowest corrosion current density values both under stationary (0.03 μA/cm^2) and friction conditions (0.8 μA/cm^2), and was characterized by both a 2–2.5 times lower wear rate (4×10^{-6} mm^3/Nm) compared to AISI 420S steel and 25TiC-Fe-CrTiNiAl and a high fracture toughness.

Keywords: electrospark deposition; composite coatings; wear resistance; corrosion resistance; artificial seawater

Citation: Kuptsov, K.A.; Antonyuk, M.N.; Sheveyko, A.N.; Bondarev, A.V.; Shtansky, D.V. Influence of TiC Addition on Corrosion and Tribocorrosion Resistance of Cr_2Ti-NiAl Electrospark Coatings. *Coatings* **2023**, *13*, 469. https://doi.org/10.3390/coatings13020469

Academic Editor: Hongbo Ju

Received: 30 January 2023
Revised: 9 February 2023
Accepted: 16 February 2023
Published: 18 February 2023

1. Introduction

Over the past decades, exploration of marine resources and development of marine industry have grown significantly. However, every year, corrosion of parts and equipment of ships and marine infrastructure leads to their premature failure, which entails significant losses as well as environmental pollution [1].

One of the most widely used materials for marine and coastal infrastructure parts is hardened stainless steel, due to its good corrosion resistance and satisfactory wear resistance [2]. The corrosion resistance of stainless steels is due to alloying with chromium, which leads to the formation of a protective passive chromium oxide film on its surface [3]. However, some loaded parts, such as pumps, valves, gears, shafts, propellers, etc., are subjected to intense friction in an aggressive corrosive environment (such as sea water), which leads to removal of the protective oxide film and, as a result, to a decrease in corrosion and wear resistance [4]. The synergistic effect of friction and corrosion is called tribocorrosion, and results in more severe equipment damage and even higher annual maintenance costs [5].

One of the most effective ways to improve the resistance of marine infrastructure parts to tribocorrosion is deposition of composite coatings consisting of a corrosion-resistant metal matrix and a hardening phase based on intermetallic compounds or transition metal carbides, which may increase the durability, reliability and service life of parts during their operation in harsh sea conditions [6,7]. As a corrosion-resistant matrix, it is preferable to use alloys with a high chromium content that are close in composition to stainless steel (Cr (12–18 wt %)) [8]. Rocha A.M.F. et al. demonstrated that the addition of Cr to the WC-FeCoNi coating significantly improved corrosion resistance [6]. Alizadeh, M et al. [7] investigated the influence of Cr on the corrosion behavior of the NiAl intermetallic compound. The increase in Cr content led to the formation of a denser Cr-based protective oxide layer on the surface which prevented formation of pitting corrosion.

In recent years, intermetallic alloys and coatings such as Ni-Ti, Ni-Al and Ti-Al have been widely used in the marine, oil, and aviation industries due to their high hardness, corrosion resistance and oxidation resistance [9,10]; moreover, these coatings have shown good tribological properties [11]. A significant disadvantage of such coatings is their high brittleness and low crack resistance [12,13], which limits their use in aggressive corrosive environments upon friction or impact loads.

One promising way to overcome this problem is to produce composite materials reinforced by elements or components with high hardness [14]. Coatings based on carbides [15,16], nitrides [17,18] and carbonitrides [19] of transition metals, such as TiC, TaC, WC, TaN, and Ti(C, N), are widely used to improve surface properties under wear and corrosion conditions, due to their high hardness, low friction coefficient and high chemical stability. Many authors have demonstrated that the introduction of such hard particles in corrosion-resistant metal matrices leads to the enhancement of hardness and strength [20], wear and erosion resistance [21], and corrosion resistance [22]. However, choosing the right hardening particles for each matrix is crucial for the corrosion behavior of the composites in terms of matching the corrosion potentials of the reinforcing particles and the metal matrix [23]. For example, the introduction of NbC (15 vol.%) particles into AISI 440 steel was shown to increase its sliding and erosion resistance, while slightly deteriorating its corrosion resistance [21]. Composite high-entropy coatings of CoCrFeNi reinforced with WC particles (up to 40 wt.%) exhibited superior wear resistance at an optimal WC content; meanwhile, a slight decrease in corrosion resistance was observed [24], and TiC-doped CoCrNiFeAl demonstrated superior corrosion resistance (1×10^{-6} A/cm^2) compared to Ti_6Al_4V substrate (1.4×10^{-4} A/cm^2) in 3.5% NaCl [25]. On the contrary, introduction of WC into a Co-Cr matrix led to a significant decrease in corrosion current density, from 3×10^{-3} to 4×10^{-4} A/cm^2, compared to non-modified Co-Cr matrix, due to the pronounced passivation effect of WC particles. However, corrosion potential decreased from 350 to 70 Mv [22].

Titanium carbide (TiC) is widely used to improve the corrosion and wear resistance of composite materials, as a hardening phase [26,27]. In our work, TiC was chosen because on the one hand, its corrosion potential is high enough to ensure effective passivation of Cr-containing metal matrix, but on the other hand, its corrosion potential is not enough to lead to pitting breakdown of the steel substrate.

Protective coatings for parts of coastal and marine infrastructure are deposited by a number of techniques such as electrospark deposition (ESD) [23,28], PCD and CVD [29,30], laser cladding [31,32], HVOF [14,33], and electroplating [34].

Original technology allowing automated electrospark deposition in a vacuum is a promising method to produce wear- and corrosion-resistant coatings on various steels and titanium alloys [35]. ESD in a vacuum allows the deposition of thick coatings (up to 200 μm) with high adhesive strength, due to the microwelding effect between the substrate and electrode material. In addition, this method is characterized by low cost, relative simplicity, and easy automation of the process, and provides the possibility of local treatment of large parts. During ESD in a vacuum, two parallel processes are implemented: classical mass transfer of yjr material from the electrode to the substrate, and pulsed cathode-arc

evaporation of the electrode, initiated by spark breakdowns. This feature increases the efficiency of the process, provides additional opportunities for doping the coating due to the use of composite cathodes, and also contributes to better surface wettability which ensures lower coating roughness. [36].The aim of this work was to obtain novel composite coatings based on a corrosion-resistant Fe-Cr_2Ti-NiAl matrix reinforced with varied content of TiC using the original technology of electrospark deposition in a vacuum, and to study the effect of TiC content on corrosion and tribocorrosion behavior in artificial seawater.

2. Experimental Details

2.1. Electrode Production

Electrodes xTiC-CrTiNiAl (x = 0, 25, 50, 75%) were manufactured from high purity Ti (PTM-1, 5–15 μm), Cr (PKh-1S, <63 μm), and NiAl (PM-NYu50, <40 μm, purity > 99%) powders that were mixed in the following atomic ratios (for x = 0): 26.7% Ti—53.4% Cr—20% NiAl. For TiC-containing electrodes, 25, 50 and 75 at.% of TiC powder was added to the initial mixture. Then, the mixtures were treated in a ball rotary mill with a drum volume of 1 L, at a mixture to balls mass ratio of 1:6 for 2 h.

Electrode bars (7 × 7 × 50 mm) were prepared by cold-pressing using a Lab Econ 600 hydraulic press (Fontijne Grotnes B.V., the Netherlands) at a pressure of 3.5 t/cm^2, and then were sintered in a high-temperature vacuum furnace VE-3-16 at a pressure of 1×10^{-3} Pa and a temperature of 1310 °C for 60 min. After sintering, the electrodes were ground to obtain rods with a diameter of 6 mm.

2.2. Coatings Deposition

The coatings were produced by a pulsed vacuum electrospark deposition (ESD) technology described elsewhere [37].

In this technology, a desktop 3D-processing CNC machine (Technologiya LLC, Russia), in which the cutter drive is replaced by a rotating electrode unit, is installed in the vacuum chamber of the UVN2 m unit. The voltage to the electrode is supplied through an insulated brush assembly. The deposition of coatings was carried out with the following constant parameters: electrode rotation speed 800 rpm, electrode movement speed 500 mm/min, surface scanning step 0.5 mm, number of passes 10 times, electric pulse frequency 100 Hz, pulse voltage 50 V and pulse duration 50 μs. The electrode with respect to the substrate was the cathode. Before ESD, the vacuum chamber was evacuated to a pressure of 10^{-3} Pa. Processing was carried out in an argon atmosphere at a pressure of 0.5 Pa.

Discs made of corrosion-resistant steel AISI 420S (ø30 × 4 mm) with roughness R_a of 6.5 μm were used as substrates.

2.3. Structure and Elemental Composition

The structure, elemental and phase composition of the electrodes and coatings were studied by scanning electron microscopy (SEM) using an S-3400N microscope (Hitachi, Tokyo, Japan) equipped with a NORAN energy-dispersive detector, and X-ray phase analysis (XRD) using a D8 Advance diffractometer (Bruker, Billerica, MA, USA) operating in a Bragg–Brentano geometry with CuKα radiation. Cross-sectional samples for SEM were mechanically cut using Secotom-50 (Struers, Denmark) and mechanically polished using Rotopol-21 (Struers, Denmark) to a roughness R_a of 20 nm. No chemical or ion etching was carried out.

Samples for TEM were produced using a FEI Helios 660 dual-beam system (Helios, NanoLab 660, FEI, USA) with a Ga^+ ion source after depositing a protective W mask. The acceleration voltage for the FIB fabrication was at 30 kV for rough operations, followed by 5 and 2 kV for final thinning. The FIB lamellae were examined using a FEI Titan Themis S/TEM microscope operating (Thermo Fisher, USA) at 300 kV. Using an energy-dispersive X-ray (EDS) Super-X Detection System with 4 SDD windowless detectors, elemental mapping of the samples was performed.

2.4. Tribocorrosion, Electrochemical and Mechanical Properties Studies

Tribocorrosion investigations of coatings and a steel substrate were carried out in artificial seawater (ASTM D 1141-98) using a tribometer (CSM Instruments, Neuchatel, Switzerland) equipped with a rotating three-electrode cell, which allowed electrochemical measurements to be carried out both under stationary conditions and during friction. This method allows effective estimation of tribocorrosive behavior of both coatings and bulk materials [38,39]. Electrochemical studies were performed using an auxiliary Pt electrode and an Ag/AgCl reference electrode. Potentiodynamic measurements both under stationary conditions and under friction conditions were carried out using a VoltaLab PST050 potentiostat (Radiometer Analytical, France), with a coating surface polarization from −200 to +700 mV relative to the open-circuit corrosion potential at a scanning rate of 1 mV/s. All potentials were recalculated relative to the standard hydrogen electrode. Corrosion current density values were calculated using Tafel equations.

Tribocorrosion studies were carried out using "ball-on-disc" scheme at a load of 5 N, a radial sliding velocity of 10 cm/s, and a run distance of 500 m. An Al_2O_3 ball with a diameter of 6 mm was used as a counterpart. Wear track profiles were studied on a Wyko-NT1100 optical profiler (Veeco, Plainview, NY, USA).

To obtain statistics, all corrosion and tribocorrosion studies were carried out using two different samples of each coating. The measurement errors did not exceed 10%.

The fatigue strength of coatings was assessed using an Impact tester (CemeCon, Germany). The tests were carried out for 10^5 cycles at a constant frequency of 50 Hz and a load of 500 N using a 5 mm in diameter WC-6Co ball. Each sample was tested in air and in artificial seawater.

Mechanical properties (hardness (H) and Young's modulus (E)) were evaluated by nanoindentation and microindentation.

Nanoindentation measurements were carried out on polished cross-sections of coatings using a TI 950 (Hysitron, Billerica, MA, USA). Before measurements, the instrument was calibrated against fused quartz. The measurements were performed in a load control mode, and maximum indentation load was set at 10 mN. The measurements' error did not exceed 10%. The loading and unloading rates were 1 mN/s, while the holding time was 2 s during nanoindentation.

Microindentation was performed on the surface of coatings using an automatic microhardness tester DuraScan 70 (EMCO-TEST Prüfmaschinen GmbH, Austria) by calculating the average value of five measurements. The maximum indentation load was set at 1 N.

3. Results and Discussion

3.1. Structure and Elemental Composition of Electrodes

Figure 1 shows SEM images of the cross-sections of Cr_2Ti-NiAl and 50%TiC-Cr_2Ti-NiAl electrodes, corresponding elemental distribution maps, as well as their composition. For both electrodes, an uneven distribution of metal elements is observed; however, TiC grains of 2–8 μm in size are distributed quite uniformly. The chemical composition of the electrodes, determined by EDS, was close to that of the initial powder mixtures.

3.2. Structure and Elemental Composition of Coatings

3.2.1. SEM

Figure 2 shows SEM images of the surface and cross-sections of the coatings with different content of titanium carbide phase (Figure 2a,b). The coatings were designated as 0TiC, 25TiC, 50TiC and 75TiC according to the content of the carbide phase in the electrodes.

The 0TiC coating deposited with a CrTi-NiAl electrode reveals many defects in the form of a cracks network (Figure 2a). Moreover, these cracks run through the entire coating thickness to the substrate (Figure 2b). The TiC-doped coatings were characterized by a defect-free and uniform morphology without noticeable pores and cracks. The thickness of all coatings did not differ much, and was in the range of 43–45 μm.

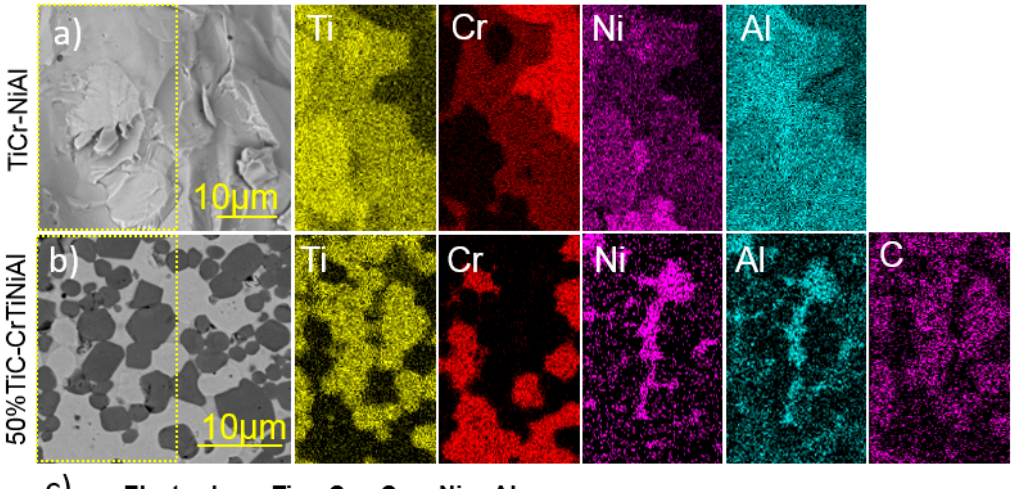

c)

Electrode	Ti	C	Cr	Ni	Al
TiCr-NiAl	26	-	42	15	17
50%TiC-CrTiNiAl	40	27	28	3	2

Figure 1. SEM images of TiCr-NiAl (**a**) and 50%TiC-CrTiNiAl (**b**) electrodes' cross-sections with corresponding EDS element distribution maps and compositions of marked areas (**c**).

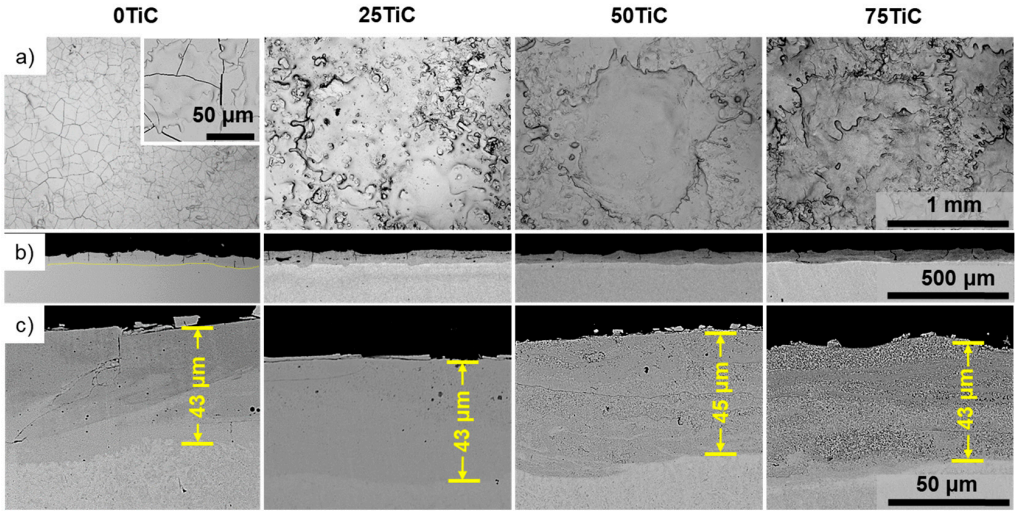

Figure 2. SEM images of surface (**a**) and cross-sections (**b**,**c**) of the coatings.

The 0TiC coating also reveals the lowest Fe content reached only 20 at.%, while carbide-modified coatings demonstrated much higher Fe content, increasing from 45 (75TiC) to 58 at.% (25TiC) (Table 1). This indicates that the introduction of carbides into the electrodes drastically changes mass transfer during the ESD process. When processing with a metallic (Cr_2Ti-NiAl) electrode, predominant electrode material transfer is observed, while in case of treatment with TiC-containing electrodes, electrode and substrate materials are mixed together in approximately equal proportions.

Table 1. Elemental composition of coatings determined by EDS (at.%).

-	C	Ti	Cr	Fe	Ni	Al
0TiC	-	18	39	20	11	12
25TiC	5	11	23	58	1	2
50TiC	9	20	21	47	1	2
75TiC	14	22	17	45	1	1

Higher magnification cross-sectional SEM images of carbide-containing coatings (Figure 3) show that the 25TiC coating is characterized by a small amount of spherical TiC particles that are 100 nm in size. An increase in the amount of carbide phase leads to a significant increase in the number and size of TiC grains (up to 200 nm) in the 50TiC coating. In some areas of the 75TiC coating, formation of dendrites up to 700 nm in size is observed, while the size of most grains do not exceed a size of 200 nm.

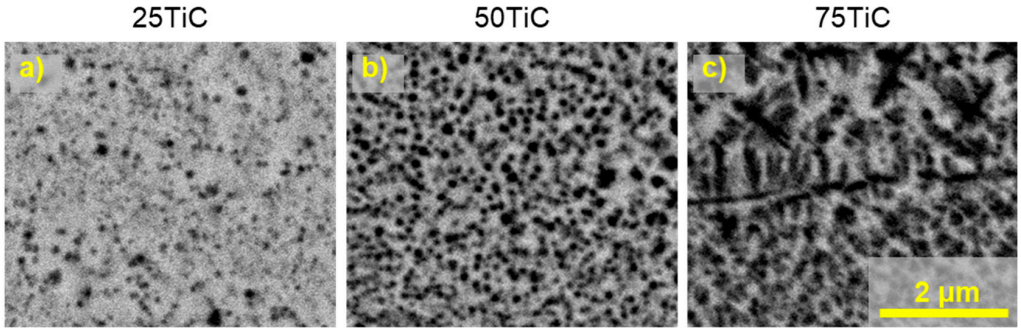

Figure 3. SEM images of cross-sections of 25TiC (**a**), 50TiC (**b**), and 75TiC (**c**) coatings at a higher magnification.

3.2.2. XRD

XRD patterns of the 0TiC, 25TiC, 50TiC, and 75TiC coatings are shown at Figure 4.

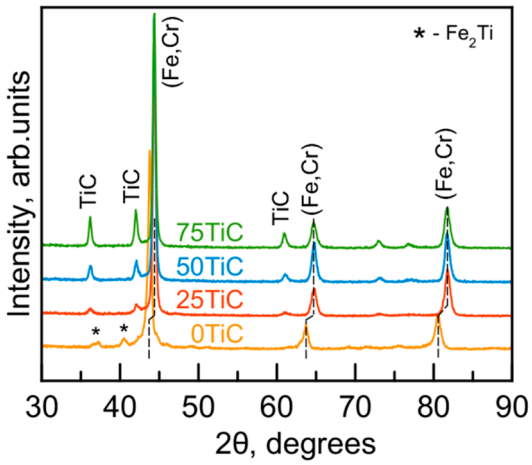

Figure 4. XRD patterns of the coatings.

The XRD pattern of the 0TiC coating has two sets of peaks. The three most intense peaks correspond to (110), (200) and (211) reflexes of a *bcc* Fe-based solid solution with a high content of alloying elements, which is evidenced by a noticeable shift of the peaks towards smaller angles (higher d-spacings). The second set of peaks corresponds to reflections from the (110) and (103) planes of the Fe_2Ti Laves phase (ICDD No. 65-0602).

XRD patterns of the carbide-containing coatings also reveal peaks from *bcc* Fe-based solid solution; however, their positions are typical of those of α-Fe and (Fe,Cr) alloys (ICDD No. 89-4186) [40]. Peaks located at around 36.2°, 42°, and 61° 2θ degrees are attributed to reflexes from (111), (200) and (220) planes of *fcc* TiC (ICDD No. 32-1383). Their intensities gradually increase with an increase in the carbide phase content of the coatings.

3.2.3. TEM

To study the coating's structure in more detail, the 75TiC coating was additionally investigated by TEM.

General views of the coating with corresponding EDS elemental distribution maps are shown in Figure 5. Carbide grains 50–200 nm in size and all elements composing the metal matrix are uniformly distributed over the coating, which agrees well with the SEM studies. It should be noted that the TiC grain size is significantly lower than that of the initial powder. This is due to the fact that carbide grains are not transferred from the electrode during ESD treatment, but precipitate from the melt formed during spark breakdowns. The content of the carbide phase in the coating was determined from the EDS elemental composition and did not exceed 30–40%.

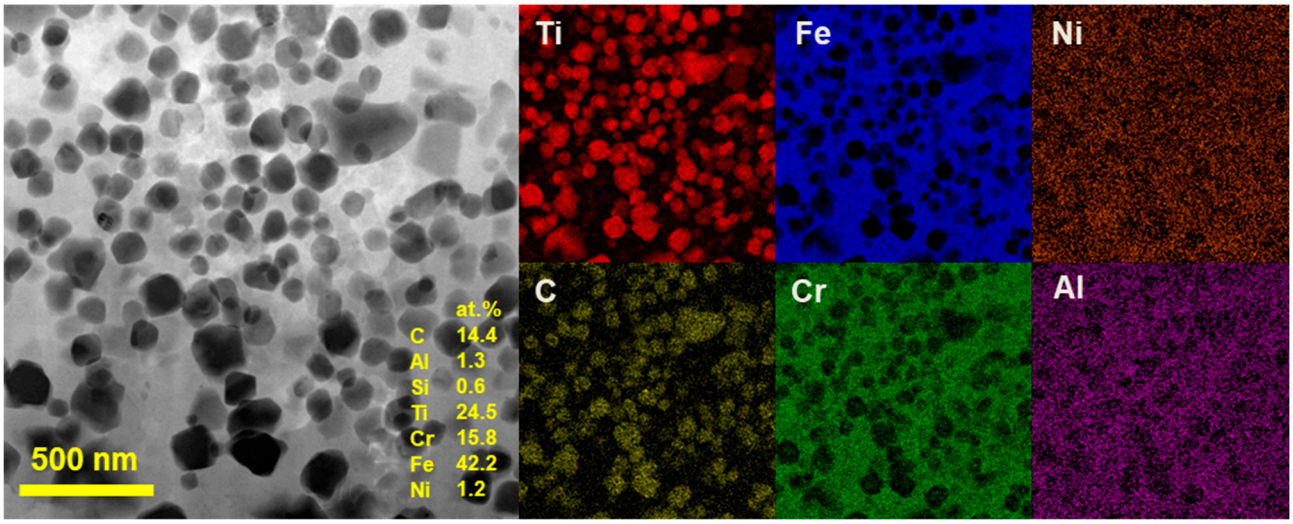

Figure 5. HAADF TEM image of 75C coating with corresponding EDS elemental maps and composition obtained from the whole area.

A number of regions including coarse TiC grains up to 500 nm in size were also observed (Figure 6). These regions were characterized by several features. Due to the high carbide phase content, the size of the matrix grains was limited to 0.5–1 μm (Figure 6a, DF). When analyzing the EDS distribution maps, a higher content of titanium was found at the grain boundaries of the matrix (Figure 6b). It was also revealed that the interfaces are characterized by lower chromium and higher nickel contents, while the iron content at the grain boundaries and in the matrix is similar. Each structural element (marked at Figure 6b as 1, 2 and 3) was additionally investigated using HR TEM and SAED methods. Dark grains (area 1) are attributed to *fcc* TiC carbide. Area 2 corresponds to (Fe, Cr) solid solution with *bcc* structure and d-spacing of 0.204 nm (110). Interestingly, Ti-rich grain boundaries were attributed to Fe_2Ti Laves phase (Figure 6e). It seems that at a small content of titanium (Ti/(Ti + Fe) < 0.3) and upon the cooling of the melt, an eutectic transformation occurs with the formation of α-Fe + Fe_2Ti mixture. Apparently, most of the Fe_2Ti was formed at a distance of at least 100–200 nm away from the carbide grains, because in their vicinity, all titanium was absorbed during TiC precipitation. Since the Fe_2Ti phase was observed in XRD pattern only for 0TiC coating, it may be assumed that the amount of that phase in the TiC-containing coatings is negligible due to a lower Ti content and a changed solidification mechanism.

3.3. Mechanical Properties

Figure 7 shows the hardness, H, and elastic modulus, E, values over the coatings' thickness, as well as their corresponding microhardness values measured on the surface of the coatings. Their nanohardness was measured on the cross-sections of the coatings at an angle to the interface from the substrate to the coating. The dashed line in Figure 7a represents the interface between the substrate and coating, while the X-axis corresponds to the distance from that interface. The hardness of the steel substrate was 5 GPa; however,

for the 0TiC coating, this value was higher (approximately 7 GPa) due to the extended transition zone. As the distance from the substrate increased, the hardness and elastic modulus increased, reaching their maximum values closer to the surface. For coating 25TiC, the hardness and elastic modulus values exhibited a plateau almost throughout the entire sample, while coatings with higher carbide content demonstrated a gradual increase in H and E values; this can be attributed to the graded TiC content in the coating increasing towards the surface. Interestingly, a maximum hardness and elastic modulus of 11.3 and 178 GPa, respectively, were observed for the 0TiC coating. Coatings with titanium carbide addition were characterized by slightly lower mechanical properties. As the content of carbide phase increased in a row of coatings 25TiC → 50TiC → 75TiC, their hardness and elastic modulus gradually increased from 8.1 to 10.3 GPa, and from 140 to 158 GPa, respectively.

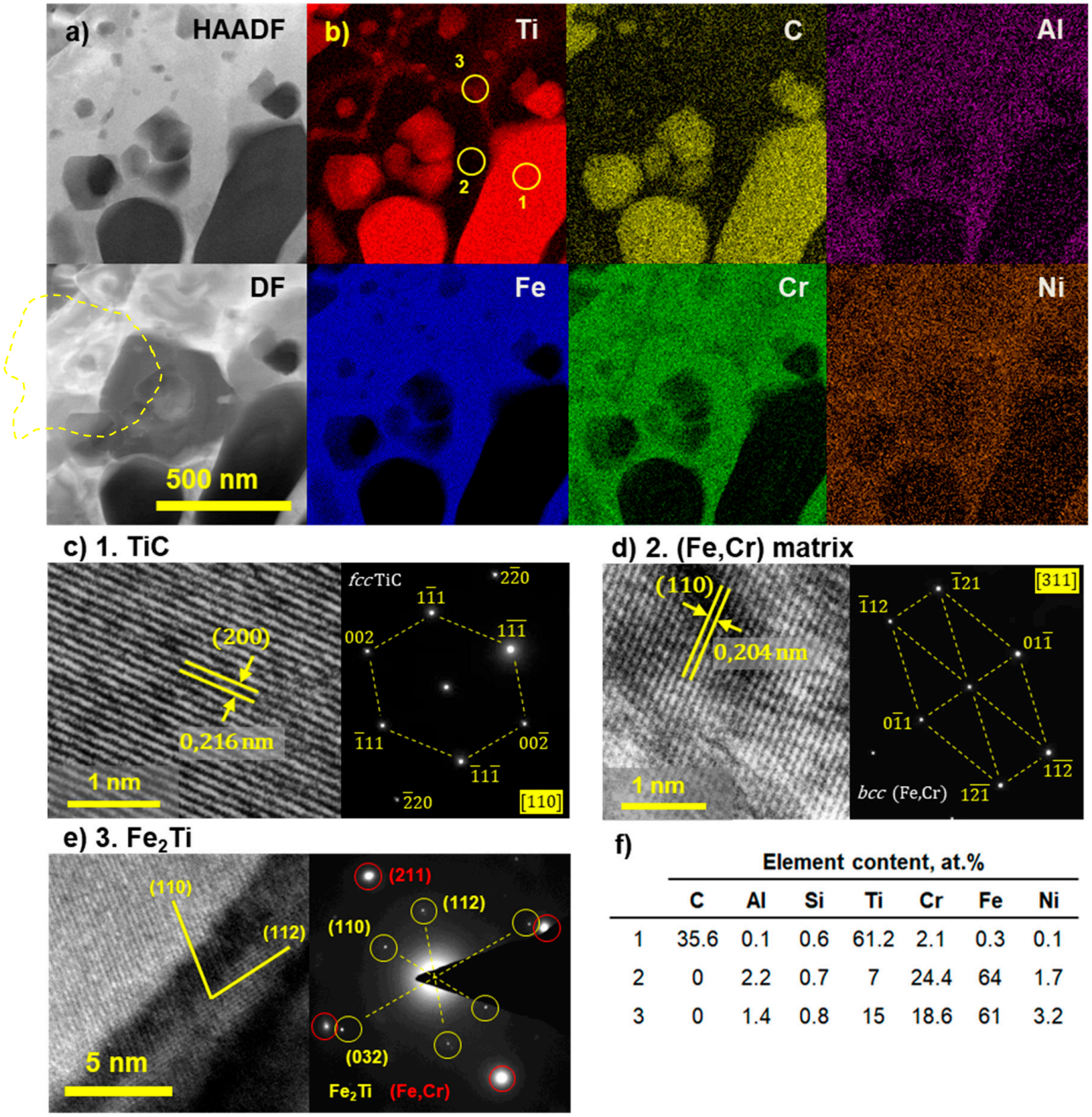

f)

	Element content, at.%						
	C	Al	Si	Ti	Cr	Fe	Ni
1	35.6	0.1	0.6	61.2	2.1	0.3	0.1
2	0	2.2	0.7	7	24.4	64	1.7
3	0	1.4	0.8	15	18.6	61	3.2

Figure 6. HAADF and DF TEM images of 75TiC coating (**a**) with EDS elemental maps (**b**) and corresponding HR TEM images, SAED patterns, and elemental composition (**f**) of marked areas 1 (**c**), 2 (**d**), and 3 (**e**).

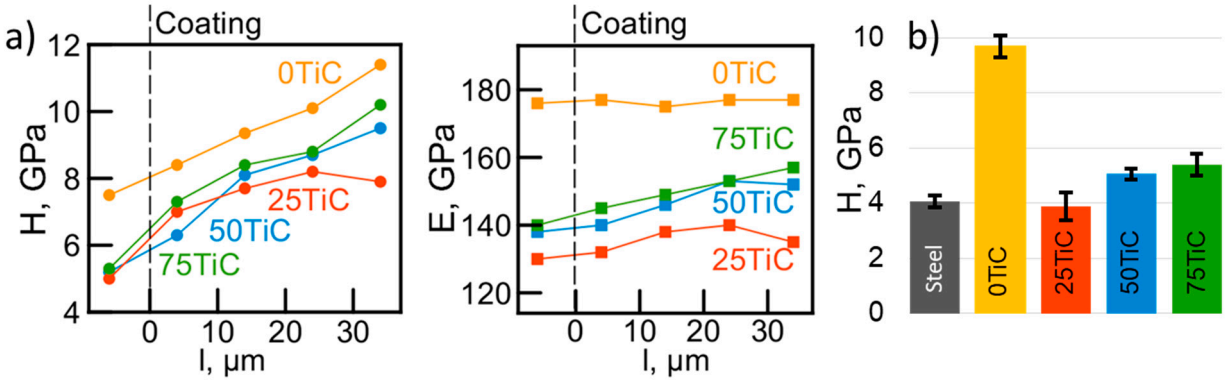

Figure 7. Results of nanoindentation (hardness, H, and elastic modulus, E) (**a**) and microhardness measurements (**b**).

The results of microhardness studies are shown in Figure 7b. The trend in microhardness corresponded to that of nanohardness (Figure 7a). A maximum hardness of 9.8 ± 0.6 GPa was observed for the 0TiC coating, while the hardness of the 25TiC, 50TiC, and 75TiC coatings gradually increased by 4 ± 0.6, 5.2 ± 0.2, and 5.5 ± 0.5 GPa, respectively. The hardness of the 420S steel substrate was 4.1 ± 0.1 GPa. The measured microhardness values are typical of those observed in TiC-reinforced composites (up to 3.6 GPa) [41]; however, coatings 50TiC and 75TiC demonstrated even higher values.

The maximum hardness observed for the 0TiC coatings without a carbide phase is probably due to a hardening caused by Fe_2Ti intermetallic inclusions [42] and a solid–solution strengthening of metal matrix [43], which has a greater effect on the hardness of coatings than inclusion of the carbide phase.

3.4. Tribocorrosion and Electrochemical Behavior of Coatings in ASW

For a detailed study of the effect of carbide phase content in coatings on their tribocorrosion behavior in ASW, several groups of experiments were carried out: (1) tribological experiments with the measurement of coefficient of friction (CoF) and open-circuit corrosion potential (OCP), (2) electrochemical experiments under stationary conditions (without friction) and (3) tribological experiments combined with electrochemical measurements (the recording of potentiodynamic curves under friction conditions).

Figure 8 shows the CoF and OCP dependences of the coatings on the running distance during tribocorrosion experiments in artificial seawater.

Before the experiment, the coatings were kept in ASW for 30 min to stabilize the OCP. After exposure, the coatings' potentials stabilized in the range of +80 (0TiC) to +190 mV (75TiC). There is a clear relationship between an increase in carbide phase content in the coatings and an increase in OCP values. This is due to a more positive potential of the carbide phase [44] and, accordingly, a more effective passivation of the surrounding metal matrix.

After exposure, the tribological part of the experiment began with simultaneous CoF and OCP values' recording. Immediately after the start of friction, a sharp drop in the potential to −100 (75TiC), −180 (50TiC) and −280 mV (25TiC) was observed, after which there was a gradual potential decrease to values of −245, −290 and −335 mV, respectively. For the TiC-free coating, a sharp drop in potential to −500 mV was observed at the initial stage, after which the potential stabilized at −300 mV until the end of the experiment. It should be noted that potential of the steel substrate during friction also reached −300 mV. Increasing the TiC content in the coatings also affects CoF and wear-rate values. Coating 0TiC demonstrated the highest CoF and wear-rate values of 0.45 and 1×10^{-5} mm^3/Nm, respectively, while 75TiC coating revealed the best tribological performance, reaching CoF and wear-rate values of 0.35 and 4×10^{-6} mm^3/Nm. Apparently, there is a clear relationship between TiC phase content and tribocorrosion behavior. Increasing the carbide phase content leads to an enhancement of mechanical properties, which has a positive effect on the wear resistance of the coatings. Uniformly distributed TiC grains protect the

metal matrix and passive layer from wear, which explains the higher potential values of the 50TiC and 75TiC coatings during friction. Additionally, TiC grains possess higher potential compared to those of the matrix, and promote matrix passivation [38]. A higher TiC grains content leads to more effective repassivation of the coatings after passive film removal during friction.

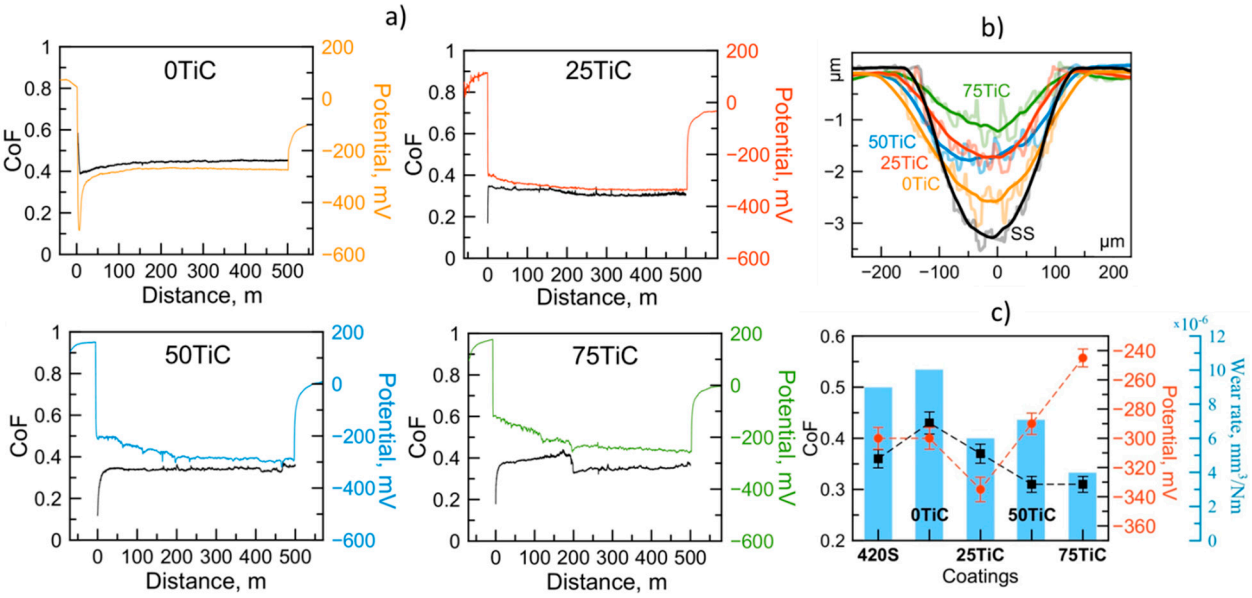

Figure 8. CoF and OCP values vs. distance of tribocorrosion tests in ASW (**a**), corresponding wear tracks profiles (**b**), and a plot summarizing CoF, average wear rates and potential values during tribological tests in ASW (**c**).

Figure 9 shows the results of electrochemical experiments on the coatings and steel substrate, performed both in steady-state and under wear conditions in ASW.

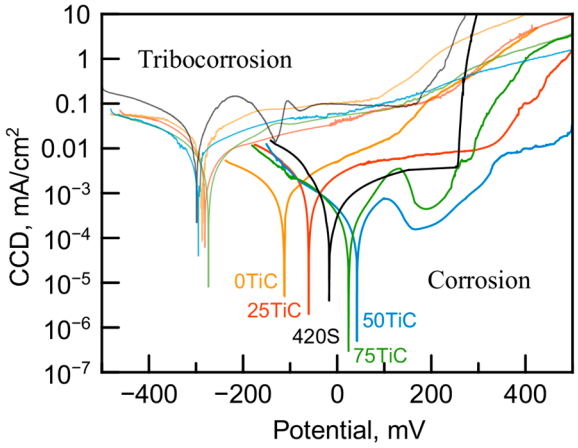

Figure 9. Potentiodynamic curves of coatings and steel substrate recorded during experiments in steady-state (corrosion) and under wear conditions (tribocorrosion).

The polarization curves, corrosion potentials and corrosion current density (CCD) values of the coatings obtained in the absence of friction (steady state) differ greatly (Table 2). First, zero current potentials are more negative than OCP. This is due to the relatively low rate of passive film formation, as there is insufficient time to form a dense layer as the potential shifts from the imposed initial cathode value. The maximum difference between these values is observed for the coating without titanium carbide (as well as for steel), and as the content of carbide increases, this difference decreases. The most negative zero current

potential is observed for the 0TiC coating, while the most positive values correspond to coatings 50TiC and 75TiC. The anodic branches of the polarization curves of the 50TiC and 75TiC coatings are characterized by a current density peak in the potential range of 100–200 mV, which is associated with the competing processes of dissolution and isolation on the surface of TiC particles by oxide.

Table 2. The corrosion potential (E_{corr}) and corrosion current density (CCD) of coatings and steel substrate measured during potentiodynamic experiments in steady-state (corrosion) and under wear conditions (tribocorrosion).

-	Corrosion		Tribocorrosion	
Material	**E_{corr}, mV**	**CCD, μA/cm^2**	**E_{corr}, mV**	**CCD, μA/cm^2**
Substrate	−25 ± 3	0.41 ± 0.06	−300 ± 26	22 ± 3
0TiC	−110 ± 6	0.22 ± 0.05	−288 ± 17	9 ± 1
25TiC	−62 ± 7	0.05 ± 0.02	−300 ± 17	6.2 ± 1
50TiC	42 ± 5	0.05 ± 0.02	−282 ± 16	4 ± 0.3
75TiC	24 ± 4	0.03 ± 0.01	−276 ± 9	0.8 ± 0.1

All the coatings do not exhibit a pronounced effect of passive film breakdown (pitting) which was observed on a steel substrate at a potential of +250 mV. Comparison of CCD shows that the metal matrix of the coatings has a slightly higher corrosion resistance compared to that of steel substrate (0.2 vs. 0.4 μA/cm^2, respectively), while the introduction of TiC into the coating composition significantly decreases CCD values to 0.05 (50TiC) and 0.03 μA/cm^2 (75TiC), demonstrating noticeable increase in the corrosion resistance. The measured CCD values are significantly lower than those up to 10 μA/cm^2, which are typically observed for TiC-based composites [41]. The anodic polarization, however, shows insufficient corrosion resistance for 0TiC and 25TiC coatings compared to steel, at least up to the breakdown potential of steel. Coatings with a high TiC content (50TiC and 75TiC) demonstrate low CCD values over the entire potential range.

Figure 10 demonstrates SEM images of wear tracks after tribocorrosion experiments. All wear tracks exhibit similar morphology but differ slightly in width, which is in consistent with the measured wear track profiles (Figure 8b). Dark pits observed both inside and outside the wear tracks are from the initial roughness of the coatings. The pits inside the wear tracks are filled with wear and corrosion products consisting mostly of Fe and Cr oxides (Figure 10e–g).

The results of combined tribological and electrochemical experiments are shown in Figure 11. Potentiodynamic measurements were carried out immediately after stabilization of the OCP and CoF at a distance of 200 m while continuing the friction. During friction, CCD values increase drastically for all the coatings by an average of 20 times (Table 2). However, the current density still tends to a decrease as the content of carbides in coatings increases. The CCD values of substrate and 0TiC coatings increased up to 22 and 9 μA/cm^2, respectively, while that of the 75TiC coating raised from 0.03 to only 0.8 μA/cm^2, evidencing the superior tribocorrosion behavior of the 75TiC coating. Zero current potential values are shifted to the negative side for all coatings, and fall within the range of −276 to −300 mV (Figure 9, Table 2). As in case of stationary electrochemical experiments, no pitting breakdown was observed during friction for all the coatings except for the steel substrate.

It worth noting an interesting feature observed for all the coatings. Under cathodic polarization, CoF is gradually increases and then reaches its maximum values (0.4–0.45) at potentials close to the transition from cathodic to anodic polarization. When the potential is shifted to more positive values, the CoF of all coatings decreases down to 0.25–0.3, which can be explained by an intense oxidation of the surface and a higher content of oxides in the wear debris. The observed effect of reducing CoF during anodic polarization is a very appealing way to increase the wear resistance of coatings capable of passivation.

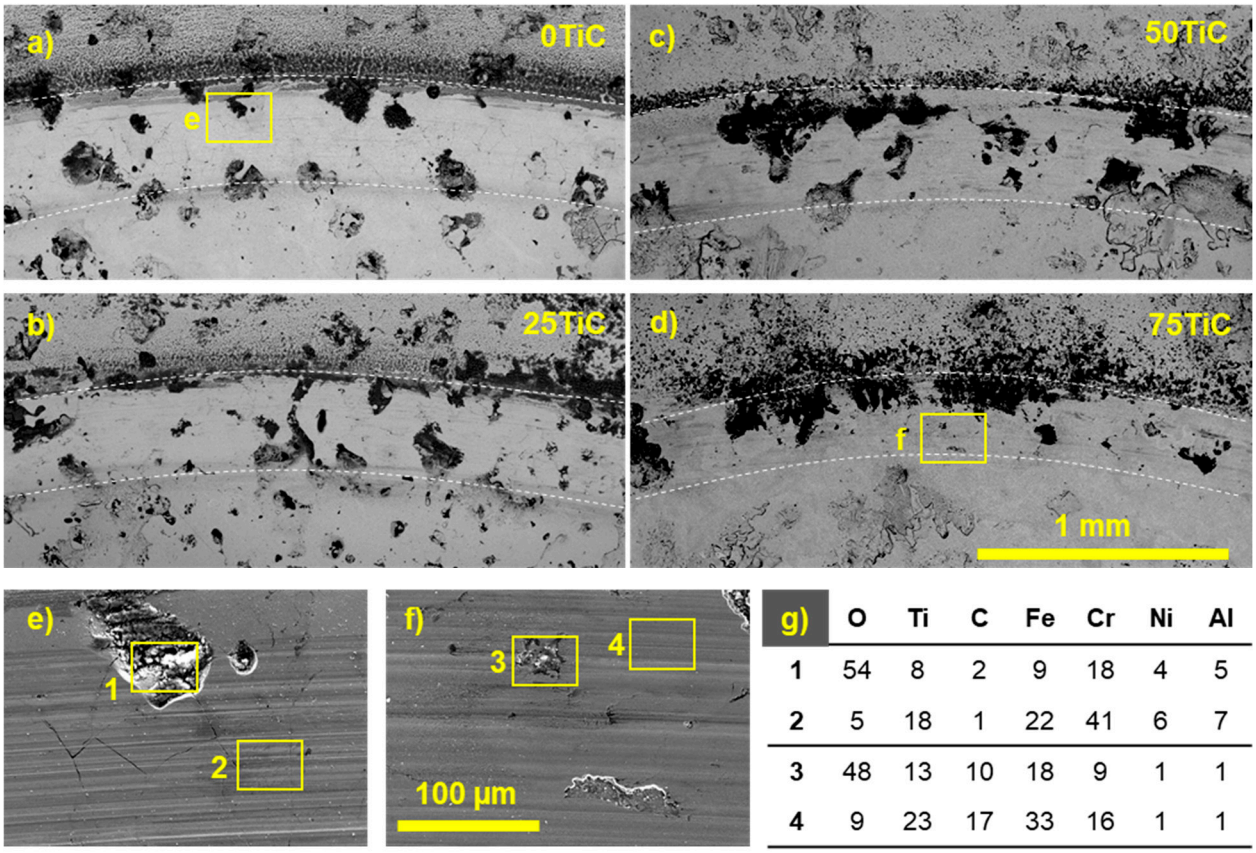

g)	O	Ti	C	Fe	Cr	Ni	Al
1	54	8	2	9	18	4	5
2	5	18	1	22	41	6	7
3	48	13	10	18	9	1	1
4	9	23	17	33	16	1	1

Figure 10. SEM images of the wear tracks on the surface of 0TiC (**a**,**e**), 25TiC (**b**), 50TiC (**c**), and 75TiC (**d**,**f**) coatings after tribocorrosion tests in ASW, as well as corresponding EDS data of marked areas (**g**).

Figure 12 shows SEM images of wear craters on coatings after impact testing in air and in artificial seawater, as well as their corresponding 2D profiles. The radius and depth of wear craters are shown in Table 3.

Table 3. Sizes (radius, R, and depth, h) of wear craters of the coatings and steel substrate after impact testing in air and in ASW.

Material	In Air		In ASW	
	R, µm	h, µm	R, µm	h, µm
Substrate	400	28	430	31
0TiC	330	15	500	39
25TiC	300	13	310	12
50TiC	320	10	310	12
75TiC	270	10	290	8

The minimum radius and depth of wear craters were observed for the coating 75TiC with the maximum carbide content, both when tested in air (270 and 10 µm) and in ASW (290 and 8 µm). As the content of the carbide phase in the coatings decreased, an increase in the size of the wear craters was observed. For example, for a 50TiC and 25TiC coating, the radii and depth of wear craters in air were 320 and 10 µm, and 280 and 13 µm, respectively, while in ASW their values were identical and equaled to 310 and 12 µm. The maximum wear crater radii among coatings were observed for the 0TiC coating both in air (330 µm) and in sea water (500 µm). Interestingly, steel substrate possessed the lowest resistance to cyclic load in air, while the 0TiC coating performed the worst in ASW, despite the highest hardness. This discrepancy is due to the fact that despite the high hardness, the 0TiC coating is characterized by a very defective structure, which led to high brittleness and

low fracture toughness in ASW experiments which are characterized by a more severe action than in air (link to our article.). The coatings with TiC were characterized by lower hardness values, but also by a high-quality defect-free structure which provided superior performance in impact testing both in air and in ASW.

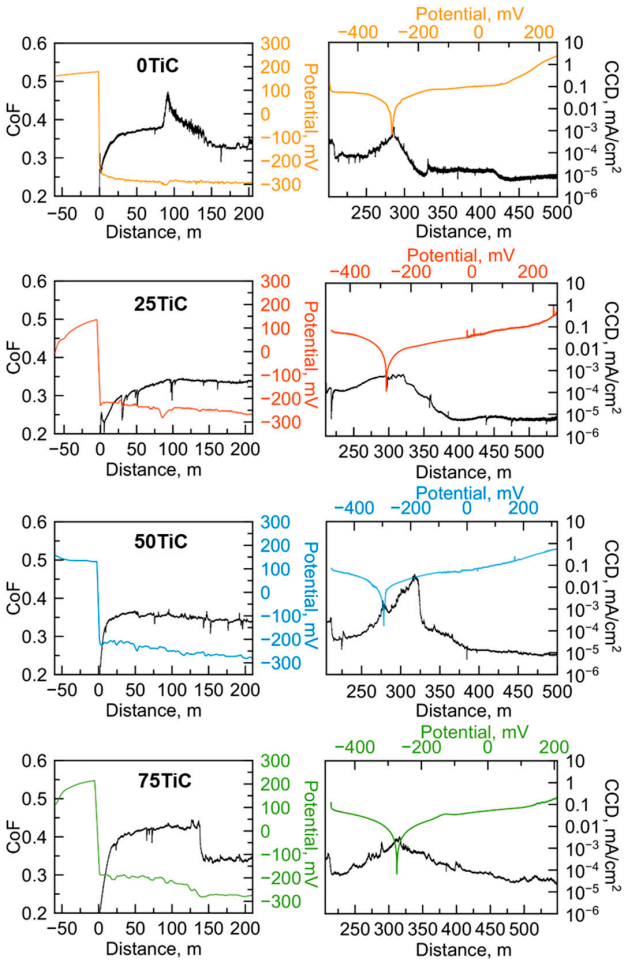

Figure 11. CoF and CCD vs. distance curves of the coatings tested against Al_2O_3 in ASW during combined tribocorrosion and electrochemical experiments.

The results of corrosion, tribocorrosion and impact tests in ASW are summarized in the scheme shown in Figure 13. The corrosion behavior of the TiC-free coating is determined by the formation of a Cr_2O_3-based passive film after the initial dissolution of iron (Figure 13a). High Cr content promotes dense and high-quality oxide layer formation.

Introduction of carbides into the coating (Figure 13b) leads to an increase in corrosion resistance via two mechanisms, which leads to more dense and thick passive film formation. First, TiC grains replace part of the surface, exposing a smaller area of the matrix. Second, TiC contributes to the enhanced passivation of the metal matrix because it has a more positive potential; however, this does not reach the repassivation potential of the metal matrix.

The protective properties of the coating under friction conditions are determined by the wear resistance of the solid phase and the rate of recovery of the passive film after its periodic removal by the counterbody and abrasive wear debris. The coating without carbide phase exhibits catastrophic wear both under friction and impact load due to high brittleness and low wear resistance. Additionally, under constant wear, passive film does not have time to recover completely between cycles (Figure 13c). A slight improvement in comparison with steel substrate is due to higher hardness and a higher content of corrosion-resistant components.

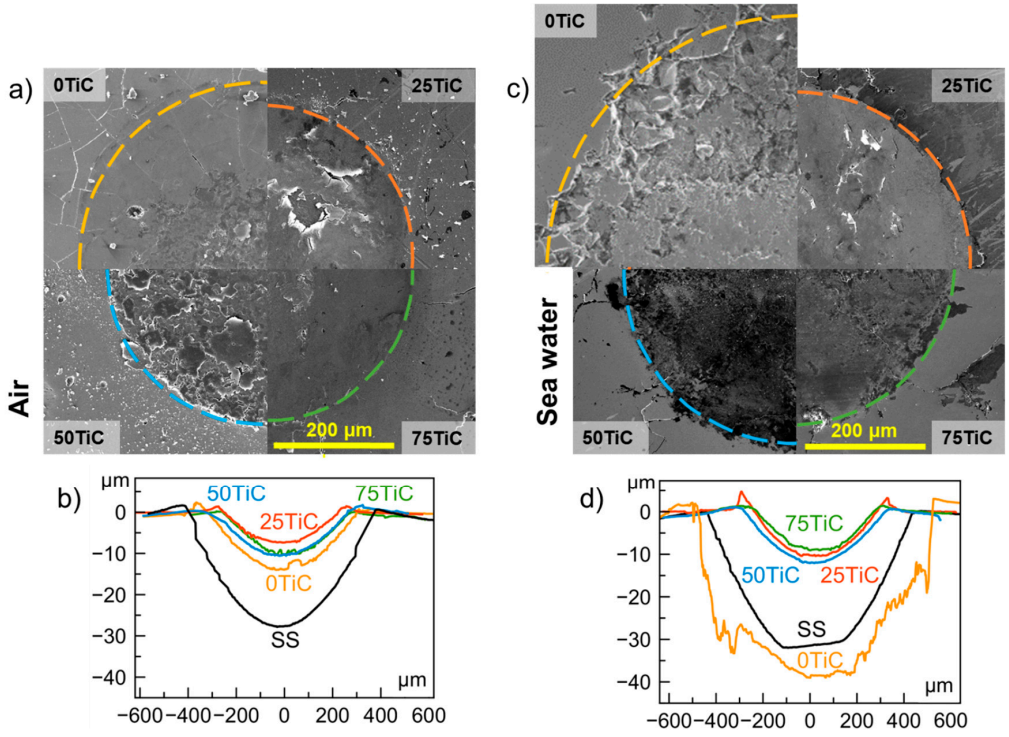

Figure 12. SEM images (**a**,**c**) and profiles of wear craters (**b**,**d**) of the coatings and steel substrate after impact testing in air and in ASW.

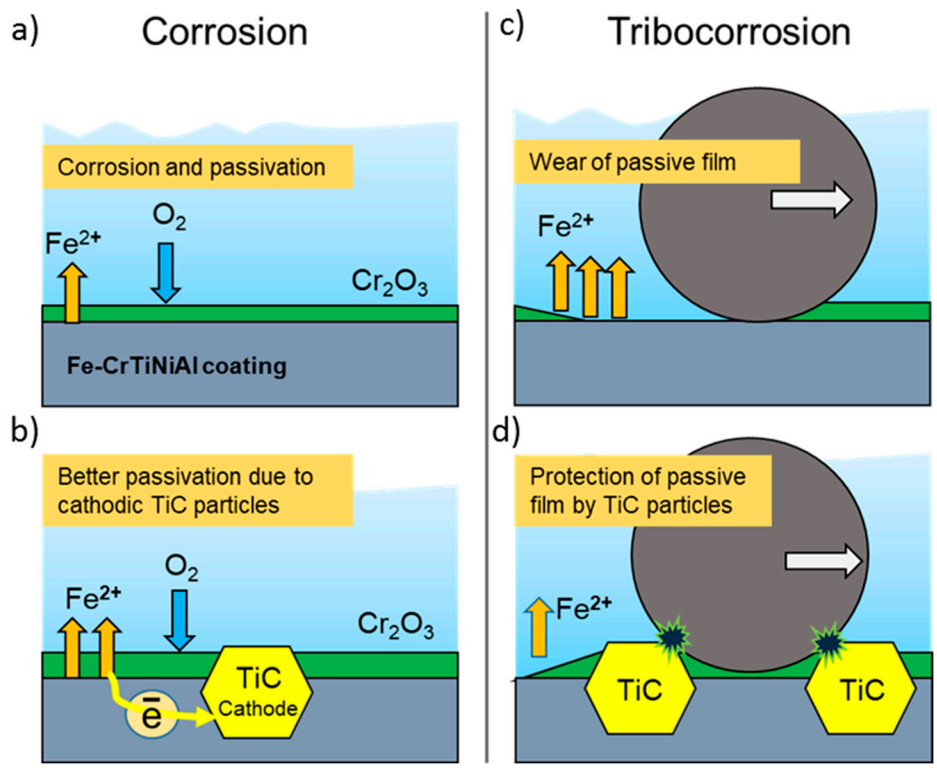

Figure 13. Scheme of TiC particles' effect on the corrosion behavior of the coatings under stationary (**a**,**c**) and wear conditions (**b**,**d**).

The best tribocorrosion behavior is demonstrated by coatings with high TiC content (Figure 13d). Under friction conditions, TiC grains, after the running-in stage, form reinforcing carcasses mainly contacting the counterbody and thereby protecting the passive

film on the metal matrix from micro-cutting [21]. The positive electrochemical potential of carbides contributes to a more efficient passive film recovery on the worn areas of metal matrix. However, an excess of the carbide component is also undesirable, since it increases the abrasiveness of wear products.

4. Conclusions

In this work, novel composite xTiC-Fe-CrTiNiAl coatings with enhanced wear and corrosion resistance were successfully produced by the original technology of electrospark deposition in a vacuum. The effect of different TiC contents on structure, mechanical properties, corrosion and tribocorrosion behavior as well as cyclic impact loads was studied in detail. The results obtained may be summarized as follows:

(1) The TiC-free Fe-CrTiNiAl coating was characterized by a defective inhomogeneous structure with a large number of transverse and longitudinal cracks and a low Fe content of 20 at.%. The introduction of carbides changed the mass transfer mechanism during electrospark deposition; namely, Fe from the substrate intermixed with the electrode material more intensively (45–58 at.%) and led to the formation of coatings with a dense uniform structure, without visible defects and with evenly distributed TiC grains.

(2) With an increase in the carbide content in electrodes, the average size and content of TiC grains in the coatings increased. The TiC-containing coatings were characterized by a hardness of 10.3 GPa and an elastic modulus of 158 GPa. The formation of a composite structure with a heavily alloyed corrosion-resistant matrix based on an α-(Fe,Cr) solid solution and uniformly distributed TiC grains (100–200 nm in size) made it possible to significantly increase resistance to stationary corrosion and tribocorrosion in artificial seawater.

(3) The TiC-free coating demonstrated increased corrosion behavior compared to AISI 420S steel, possessing j_{corr} values of 0.2 and 9 $\mu A/cm^2$ under stationary and wear conditions compared to those of steel substrate (0.41 and 22 $\mu A/cm^2$); however, no enhancement of wear resistance was observed.

(4) Introduction of TiC led to a significant increase both in corrosion and tribocorrosion behavior. The best 75TiC-Cr_2Ti-NiAl coating demonstrated the lowest corrosion current densities both under stationary conditions (0.03 $\mu A/cm^2$) and under friction conditions (0.8 $\mu A/cm^2$). In addition, this coating was characterized by the lowest wear rate (4×10^{-6} mm^3/Nm vs. 1×10^5 mm^3/Nm of TiC-free coating), a high resistance to cyclic impact loads (500 N, 10^5 cycles), the lowest potential shift during tribocorrosion (down to −240 mV compared to −340 mV for 25TiC-Fe-CrTiNiAl) and the fastest rate of recovery of the passive film under friction conditions.

(5) The mechanism of the enhancement of the corrosion and tribocorrosion behavior of the TiC-containing coatings was explained. Under stationary conditions, corrosion resistance is determined by high Cr content in the metal matrix and by TiC-induced passivation; meanwhile, under wear conditions, TiC particles acted as a reinforcing carcass, protecting the passive layer on metal matrix and promoting effective passivation of worn areas.

Author Contributions: Conceptualization, K.A.K. and A.N.S.; investigation, K.A.K., A.N.S., M.N.A. and A.V.B.; writing—original draft, M.N.A. and K.A.K.; writing—review and editing, D.V.S. and K.A.K.; visualization, K.A.K. and M.N.A.; supervision, K.A.K. and D.V.S.; project administration, K.A.K.; funding acquisition, K.A.K. All authors have read and agreed to the published version of the manuscript.

Funding: This work was financially supported by the Russian Science Foundation (Agreement No. 20-79-10104).

Institutional Review Board Statement: Not applicable.

Informed Consent Statement: Not applicable.

Data Availability Statement: Not applicable.

Acknowledgments: AVB acknowledges CzechNanoLab Research Infrastructure, supported by MEYS CR (LM2018110) for TEM investigations.

Conflicts of Interest: The authors declare no conflict of interest.

Abbreviations

CCD	Corrosion current density
OCP	Open-circuit corrosion potential
CoF	Coefficient of friction
ESD	Electrospark deposition
ASW	Artificial seawater
XRD	X-ray diffraction
SEM	Scanning electron microscopy
TEM	Transmitting electron microscopy
HAADF	High-angle annular dark field
EDS	Energy dispersive X-ray spectroscopy
SAED	Selected area electron diffraction
HR	TEM high resolution transmitting electron microscopy
DF	Dark field

References

1. Castro, J.D.; Lima, M.J.; Carvalho, S. Corrosion Resistance of Cu-Zr(O) N Films in a Simulated Seawater Environment. *Surf. Coat. Technol.* **2022**, *451*, 129050. [CrossRef]
2. Liu, W.; Yang, H.; Li, X.; Zhang, Z.; Lin, Y.; Deng, K. Effect of Chloride and Iodide on the Corrosion Behavior of 13Cr Stainless Steel. *Metals* **2022**, *12*, 1833. [CrossRef]
3. Olsson, C.O.A.; Landolt, D. Passive Films on Stainless Steels—Chemistry, Structure and Growth. *Electrochim. Acta* **2003**, *48*, 1093–1104. [CrossRef]
4. Wood, R.J.K. Marine Wear and Tribocorrosion. *Wear* **2017**, *376–377*, 893–910. [CrossRef]
5. Hoque, M.A.; Yao, C.W.; Khanal, M.; Lian, I. Tribocorrosion Behavior of Micro/Nanoscale Surface Coatings. *Sensors* **2022**, *22*, 9974. [CrossRef]
6. Rocha, A.M.F.; Bastos, A.C.; Cardoso, J.P.; Rodrigues, F.; Fernandes, C.M.; Soares, E.; Sacramento, J.; Senos, A.M.R.; Ferreira, M.G.S. Corrosion Behaviour of WC Hardmetals with Nickel-Based Binders. *Corros. Sci.* **2019**, *147*, 384–393. [CrossRef]
7. Alizadeh, M.; Mohammadi, G. Effect of Micro-Alloying Chromium on the Corrosion Resistance of Nanocrystalline Nickel Aluminide Intermetallic Produced by Mechanical Alloying Process. *Mater. Lett.* **2012**, *67*, 148–150. [CrossRef]
8. Cihangir, S.; Say, Y.; Ozkul, İ.; Guler, O.; Guler, S.H. Microstructure and Corrosion Investigation of $FeCoCrNiMo_{0,5}(MnAl)_{0,3}$ High Entropy Alloy Produced by 316 L Stainless Steel Scrap. *Mater. Today Commun.* **2022**, *33*, 104360. [CrossRef]
9. Lin, C.; Wu, W.; Han, Y.; Liu, J.; Zhang, M.; Wang, Q.; Li, X. Orderly Nucleation and Competitive Growth Behaviors of Ti-Al Intermetallic Compounds in Ti/TiAl3 Diffusion Couple under High Temperature. *J. Alloy. Compd.* **2023**, *939*, 168815. [CrossRef]
10. Singh, A.P.; Srivastava, C. Understanding the Non-Monotonic Variation in the Corrosion Rate of Sn-Ni Coatings with Ni Addition by the Analysis of Texture and Grain Boundary Constitution of the Matrix Phase and Spatial Distribution of the Intermetallic Phase in the Coating Microstructure. *Corros. Sci.* **2023**, *211*, 110787. [CrossRef]
11. Cai, C.; Song, B.; Wei, Q.; Xue, P.; Wen, S.; Liu, J.; Shi, Y. In-Situ Integrated Fabrication of Ti–Ni Coating during Hot Isostatic Pressing of Ti6Al4V Parts: Microstructure and Tribological Behavior. *Surf. Coat. Technol.* **2015**, *280*, 194–200. [CrossRef]
12. Chen, Y.; Niu, H.; Kong, F.; Xiao, S. Microstructure and Fracture Toughness of a β Phase Containing TiAl Alloy. *Intermetallics* **2011**, *19*, 1405–1410. [CrossRef]
13. Yokoshima, S.; Yamaguchi, M. Fracture Behavior and Toughness of PST Crystals of TiAl. *Acta Mater.* **1996**, *44*, 873–883. [CrossRef]
14. Ahledel, N.; Schulz, R.; Gariepy, M.; Hermawan, H.; Alamdari, H. Electrochemical Corrosion Behavior of Fe3Al/TiC and Fe3Al-Cr/TiC Coatings Prepared by HVOF in NaCl Solution. *Metals* **2019**, *9*, 437. [CrossRef]
15. Bin Humam, S.; Gyawali, G.; Amanov, A.; Kim, T.H.; Lee, S.W. Microstructure, Interface, and Nanostructured Surface Modifications to Improve Mechanical and Tribological Performance of Electrodeposited Ni-W-TaC Composite Coating. *Surf. Coat. Technol.* **2021**, *419*, 127293. [CrossRef]
16. Wang, Q.; Luo, S.; Wang, S.; Wang, H.; Ramachandran, C.S. Wear, Erosion and Corrosion Resistance of HVOF-Sprayed WC and Cr3C2 Based Coatings for Electrolytic Hard Chrome Replacement. *Int. J. Refract. Met. Hard Mater.* **2019**, *81*, 242–252. [CrossRef]
17. Santaella-González, J.B.; Hernández-Torres, J.; Morales-Hernández, J.; Flores-Ramírez, N.; Ferreira-Palma, C.; Rodríguez-Jiménez, R.C.; García-González, L. Effect of the Number of Bilayers in Ti/TiN Coatings on AISI 316L Deposited by Sputtering on Their Hardness, Adhesion, and Wear. *Mater. Lett.* **2022**, *316*, 132037. [CrossRef]
18. Fang, J.; Piliptsou, D.G.; Bekarevich, R.; Rogachev, A.V.; Jiang, X.; Kulesh, E. Effect of the Alloying Elements in TiN Sublayer on the Structure and Mechanical Properties of Carbon Coatings. *Thin Solid Films* **2022**, *755*, 139324. [CrossRef]
19. Ou, Y.X.; Wang, H.Q.; Hua, Q.S.; Liao, B.; Ouyang, X.P. Tribocorrosion Behaviors of Superhard yet Tough Ti-C-N Ceramic Coatings. *Surf. Coat. Technol.* **2022**, *439*, 128448. [CrossRef]

20. Zou, Y.; Tan, C.; Qiu, Z.; Ma, W.; Kuang, M.; Zeng, D. Additively Manufactured SiC-Reinforced Stainless Steel with Excellent Strength and Wear Resistance. *Addit. Manuf.* **2021**, *41*, 101971. [CrossRef]
21. Kan, W.H.; Proust, G.; Bhatia, V.; Chang, L.; Dolman, K.; Lucey, T.; Tang, X.; Cairney, J. Slurry Erosion, Sliding Wear and Corrosion Behavior of Martensitic Stainless Steel Composites Reinforced in-Situ with NbC Particles. *Wear* **2019**, *420–421*, 149–162. [CrossRef]
22. Wang, X.; Wang, M.; Yi, H.; García, J.L.; Wang, X.; Wang, M. Research on the Preparation Process and Performance of a Wear-Resistant and Corrosion-Resistant Coating. *Crystals* **2022**, *12*, 591. [CrossRef]
23. Antonyuk, M.N.; Kuptsov, K.A.; Sheveyko, A.N.; Shtansky, D.V. Antibacterial TaC-(Fe,Cr,Mo,Ni)-(Ag/Cu) Composite Coatings with High Wear and Corrosion Resistance in Artificial Seawater. *Lubricants* **2022**, *10*, 320. [CrossRef]
24. Wu, T.; Chen, Y.; Lin, B.; Yu, L.; Gui, W.; Li, J.; Wu, Y.; Zeng, D. Effects of WC on the Microstructure, Wear and Corrosion Resistance of Laser-Deposited CoCrFeNi High Entropy Alloy Coatings. *Coatings* **2022**, *12*, 985. [CrossRef]
25. Li, W.; Li, J.; Xu, Y. Investigation into the Corrosion Wear Resistance of CoCrFeNiAlx Laser-Clad Coatings Mixed with the Substrate. *Metals* **2022**, *12*, 460. [CrossRef]
26. Tang, M.; Zhang, L.; Zhang, N. Microstructural Evolution, Mechanical and Tribological Properties of TiC/Ti6Al4V Composites with Unique Microstructure Prepared by SLM. *Mater. Sci. Eng. A* **2021**, *814*, 141187. [CrossRef]
27. Günen, A.; Soylu, B.; Karakaş, Ö. Titanium Carbide Coating to Improve Surface Characteristic, Wear and Corrosion Resistance of Spheroidal Graphite Cast Irons. *Surf. Coat. Technol.* **2022**, *437*, 128280. [CrossRef]
28. Kayalı, Y.; Kanca, E.; Günen, A. Effect of Boronizing on Microstructure, High-Temperature Wear and Corrosion Behavior of Additive Manufactured Inconel 718. *Mater. Charact.* **2022**, *191*, 112155. [CrossRef]
29. Siddiqui, A.R.; Maurya, R.; Katiyar, P.K.; Balani, K. Superhydrophobic, Self-Cleaning Carbon Nanofiber CVD Coating for Corrosion Protection of AISI 1020 Steel and AZ31 Magnesium Alloys. *Surf. Coat. Technol.* **2020**, *404*, 126421. [CrossRef]
30. Liao, L.; Gao, R.; Yang, Z.H.; Wu, S.T.; Wan, Q. A Study on the Wear and Corrosion Resistance of High-Entropy Alloy Treated with Laser Shock Peening and PVD Coating. *Surf. Coat. Technol.* **2022**, *437*, 128281. [CrossRef]
31. Feng, J.; Xiao, H. Tribocorrosion Behavior of Laser Cladded Ti-Al-(C, N) Composite Coatings in Artificial Seawater. *Coatings* **2022**, *12*, 187. [CrossRef]
32. Aubry, P.; Blanc, C.; Demirci, I.; Gorny, C.; Maskrot, H. Analysis of a Ni-Fe-Cr-Mo-Si Hardfacing Alloy Manufactured by Laser Cladding: Influence of the Iron Content on the Wear Resistance Properties. *Procedia CIRP* **2018**, *74*, 210–213. [CrossRef]
33. Brezinová, J.; Landová, M.; Guzanová, A.; Dulebová, L.; Draganovská, D. Microstructure, Wear Behavior and Corrosion Resistance of WC-FeCrAl and WC-WB-Co Coatings. *Metals* **2018**, *8*, 399. [CrossRef]
34. Klekotka, M.; Zielińska, K.; Stankiewicz, A.; Kuciej, M. Tribological and Anticorrosion Performance of Electroplated Zinc Based Nanocomposite Coatings. *Coatings* **2020**, *10*, 594. [CrossRef]
35. Kuptsov, K.A.; Kiryukhantsev-Korneev, P.V.; Sheveyko, A.N.; Shtansky, D.V. Comparative Study of Electrochemical and Impact Wear Behavior of TiCN, TiSiCN, TiCrSiCN, and TiAlSiCN Coatings. *Surf. Coat. Technol.* **2013**, *216*, 273–281. [CrossRef]
36. Kuptsov, K.A.; Sheveyko, A.N.; Manakova, O.S.; Sidorenko, D.A.; Shtansky, D.V. Comparative Investigation of Single-Layer and Multilayer Nb-Doped TiC Coatings Deposited by Pulsed Vacuum Deposition Techniques. *Surf. Coat. Technol.* **2020**, *385*, 125422. [CrossRef]
37. Kuptsov, K.A.; Sheveyko, A.N.; Zamulaeva, E.I.; Sidorenko, D.A.; Shtansky, D.V. Two-Layer Nanocomposite WC/a-C Coatings Produced by a Combination of Pulsed Arc Evaporation and Electro-Spark Deposition in Vacuum. *Mater. Des.* **2019**, *167*, 107645. [CrossRef]
38. Kuptsov, K.A.; Sheveyko, A.N.; Sidorenko, D.A.; Shtansky, D.V. Electro-Spark Deposition in Vacuum Using Graphite Electrode at Different Electrode Polarities: Peculiarities of Microstructure, Electrochemical and Tribological Properties. *Appl. Surf. Sci.* **2021**, *566*, 150722. [CrossRef]
39. Pezzato, L.; Vranescu, D.; Sinico, M.; Gennari, C.; Settimi, A.G.; Pranovi, P.; Brunelli, K.; Dabalà, M. Tribocorrosion Properties of PEO Coatings Produced on AZ91 Magnesium Alloy with Silicate- or Phosphate-Based Electrolytes. *Coatings* **2018**, *8*, 202. [CrossRef]
40. Petrov, Y.I.; Shafranovsky, E.A.; Krupyanskii, Y.F.; Essine, S.V. Structure and Mössbauer Spectra for the Fe–Cr System: From Bulk Alloy to Nanoparticles. *J. Appl. Phys.* **2001**, *91*, 352. [CrossRef]
41. Tornabene, F.; Lu, C.-J.; Yeh, J.-W. Improved Wear and Corrosion Resistance in TiC-Reinforced SUS304 Stainless Steel. *J. Compos. Sci.* **2023**, *7*, 34. [CrossRef]
42. Sheveyko, A.N.; Kuptsov, K.A.; Kiryukhantsev-Korneev, P.V.; Kaplansky, Y.Y.; Orekhov, A.S.; Levashov, E.A. Protective Coatings for LPBF Ni-Based Superalloys Using a Combination of Electrospark Deposition and Pulsed Arc Evaporation Methods. *Appl. Surf. Sci.* **2022**, *581*, 152357. [CrossRef]
43. Zhang, J.; Xin, S.; Zhang, Y.; Guo, P.; Sun, H.; Li, T.; Qin, C. Effects of Elements on the Microstructure and Mechanical Properties of AlCoCrFeNiTi High-Entropy Alloys. *Metals* **2023**, *13*, 178. [CrossRef]
44. Memarrashidi, Z.; Plucknett, K.P. The Effects of C:N Ratio on the Aqueous Corrosion Response of TiC and Ti(C,N) Cermets with a Ni3Al-Based Binder. *Int. J. Refract. Met. Hard Mater.* **2016**, *61*, 162–172. [CrossRef]